Journal of Geophysical Research: Oceans

RESEARCH ARTICLE
10.1029/2018JC013894

Sediment Dynamics in Wind Wave-Dominated Shallow-Water Environments

K. S. Nelson[1] and O. B. Fringer[1]

[1]The Bob and Norma Street Environmental Fluid Mechanics Laboratory, Stanford University, Stanford, CA, USA

Key Points:
- Wind waves over smooth beds can decrease vertical momentum fluxes resulting in reduced bottom roughness and drag
- Through direct numerical simulation, we show wind waves control sediment entrainment, but currents are necessary for vertical mixing
- Currents affect the magnitude and duration of sediment entrainment throughout the wave cycle, but not phasing of the bed shear stress

Correspondence to:
K. S. Nelson,
knelson3@stanford.edu

Citation:
Nelson, K. S., & Fringer, O. B. (2018). Sediment dynamics in wind wave-dominated shallow-water environments. *Journal of Geophysical Research: Oceans*, *123*, 6996–7015. https://doi.org/10.1029/2018JC013894

Received 8 FEB 2018
Accepted 3 JUL 2018
Accepted article online 20 JUL 2018
Published online 1 OCT 2018

Abstract Sediment dynamics driven by waves and currents in shallow-water estuarine environments impacts many physical and biological processes and is important to the estuary-wide sediment budget. Observational restrictions have limited our ability to understand the physics governing sediment entrainment and mixing in these environments. To this end, we use direct numerical simulation to simulate sediment transport processes in shallow, combined wave- and current-driven flows. Simulations are run with depth-averaged currents ranging from 0 to 9 cm/s, while wave conditions are held constant with a bottom orbital velocity and period of 10 cm/s and 3 s, respectively. Our results indicated that for wave-dominated conditions, waves reduce vertical momentum fluxes and the associated bottom drag, thereby accelerating mean currents. Conversely, currents do not significantly affect the wave velocity field. However, they increase the bed shear stress and change the timing and duration of sediment entrainment throughout the wave cycle. Counterintuitively, these effects lead to lower suspended sediment concentrations near the bed for a portion of the wave cycle. By analyzing sediment fluxes, waves are shown to drive near-bed sediment dynamics while currents control vertical mixing above the buffer layer, where downward settling is predominantly balanced by the current-generated vertical turbulent sediment flux. In the absence of currents, sediment concentrations are negligible above the wave boundary layer because mixing is weak. We show that the time- and phase-averaged sediment concentration profiles for wave and current conditions resemble the theoretical Rouse profile derived for equilibrium conditions in statistically steady, unidirectional turbulent channel flow.

Plain Language Summary The transport of mass, such as nutrients and sediment, by fluid flows is fundamental to aquatic life and is crucial to many environmental and coastal engineering studies. Whether predicting the dispersion of shrimp larvae or assessing the mobilization of sediment-sorbed contaminants, the fluid mechanics governing the transport processes is the most important underlying physical phenomenon. Despite its importance, many mechanisms controlling the movement of sediment in estuaries are poorly understood. This is particularly true near the sediment bed where our ability to observe and measure properties relevant to the physics is limited. To this end, we apply state-of-the-art supercomputers to simulate sediment transport by fluid flow in environments with waves and currents. Contrary to popular belief within the fluid mechanics community, we find that currents can accelerate in the presences of waves. This acceleration can potentially affect how sediment and nutrients move within an estuary. Currents also affect the duration and magnitude of sediment erosion. Our results support the conceptual model that wind-generated waves strongly influence sediment erosion, but currents are required to mix sediment into the water column. Ultimately, our work gives better insight into the mechanisms controlling sediment transport in estuaries which can impact water quality management.

1. Introduction

Sediment plays a crucial role in many physical and biological processes within aquatic systems and affects the fate and transport of aqueous contaminants by controlling the availability of heavy metals and other organic pollutants (Lick, 2008). Suspended sediment in estuaries has also been long recognized to regulate the growth of phytoplankton by controlling light availability (Cloern, 1987; Colijn, 1982; Kirk, 1985). In addition to its importance to water quality, sediment transport processes such as erosion and accretion dictate the health, stability, and shape (Friedrichs, 2011; Jones & Jaffe, 2013) of wetlands and intertidal mud flats, both of which are ecologically critical habitats. The fundamental role sediment plays within physical and biological

estuarine systems necessitates the need for policy and decisions makers to understand sediment transport processes.

Sediment in estuaries is typically riverine in origin but often has residence times on the order of decades, redistributing within and between habitats repeatedly. Waves and tidal currents are the primary mechanisms driving the redistribution. Short period (1–5 s), locally generated wind waves are effective at suspending sediment in shallow intertidal mudflats. In the Upper Chesapeake Bay, for example, wind wave sediment suspension often exceeds current suspension by a factor of 3–5 (Sanford, 1994). Similarly in South San Francisco Bay, shallow-water (depth less than 2 m) suspended sediment concentrations (SSCs) were observed to increase from 30 mg/L during calm periods to over 100 mg/L during wavy periods (Brand et al., 2010). Once suspended, lateral fluxes caused by winds (Chen et al., 2009), tides (Pritchard & Hogg, 2003), or baroclinic forcings (Lacy et al., 2014) can transport sediment from the shallows to neighboring channels. The channels then act as conduits allowing advection by tidal currents, where sediment can remain suspended for a significant portion of the tidal cycle leading to widespread sediment dispersal (Christie et al., 1999; Dyer et al., 2000).

Although decades of research has increased our knowledge of large-scale sediment transport in estuaries, we do not fully understand the physics governing sediment entrainment (mobilization of sediment from the bed into the water column) and mixing. As pointed out in the review article on wave-driven sediment suspension and transport processes by Green and Coco (2014), our knowledge of sediment dynamics in estuaries is largely empirical and based primarily on observations in the form of time series. Practical restrictions have limited the spatial and temporal resolution of these observations, making it difficult to understand intricacies governing the physics. The hydrodynamics alone is complex when waves and currents coexist because of nonlinear coupling of the wave and current boundary layers.

It is well established that a fully turbulent wave boundary layer will increase the resistance of overlying currents. Grant and Madsen (1979) formulated a model that parameterized this effect by introducing an *apparent roughness*, which represents the increased roughness scale felt by currents because of wave-enhanced dissipation near the sediment bed. Various extensions (e.g., Glenn & Grant, 1987; Styles & Glenn, 2000) of this model have been proposed that also include the effects of sediment-induced stratification. Although these models and many others (Christoffersen & Jonsson, 1985; Styles et al., 2017) provide rich information about wave, current, and sediment interactions, they often assume a fully turbulent wave boundary layer with mixing represented by a time-invariant eddy viscosity and that the sediment bed is hydraulically rough (e.g., Glenn & Grant, 1987; Grant & Madsen, 1979; Styles et al., 2017). Although these assumptions are valid for high Reynolds number waves over sandy bottoms, they do not always apply to estuarine conditions.

Estuaries often contain silts and clays with grain sizes much smaller than the viscous sublayer thickness, implying a hydraulically smooth bed. Furthermore, wind waves in estuaries are typically short period (1–5 s) (Green & Coco, 2014) and relatively small (typically <0.5 m ; Brand et al., 2010; Lacy et al., 2014; MacVean & Lacy, 2014), resulting in Stokes Reynolds numbers less than 200. Wave boundary layers with such low Reynolds numbers over smooth beds are laminar (Hino et al., 1976).

In contrast to the effects of oscillatory flows with high Reynolds numbers, experimental pipe flow studies have shown that low Reynolds number oscillations can reduce turbulence in combined flows (Lodahl et al., 1998). Stabilizing effects from flow oscillation on the transition to turbulence are also well reported in the literature (Ramaprian & Tu, 1980; Sarpkaya, 1966; Singer et al., 1989). Lodahl et al. (1998) showed that currents can be laminarized by flow oscillations if the flow is *wave dominated* (i.e., bottom orbital velocity exceeds the depth-averaged currents) and the oscillatory component is laminar. More recently, direct numerical simulation (DNS) was applied to study period- (Manna et al., 2012) and phase-averaged (Manna et al., 2015) turbulent statistics for wave-dominated pulsating pipe flows. The oscillating pressure gradient was found to weaken turbulence and transferred turbulent kinetic energy from the streamwise to spanwise components.

Low Reynolds number waves can dominate over currents in shallow-water estuarine environments where bottom orbital velocities can exceed mean currents during windy events (e.g., Brand et al., 2010; MacVean & Lacy, 2014). However, the implication of this regime and the intricacies governing the wave, current, and sediment interaction in the resulting wave and current boundary layer are not well reported in the literature. This gap is in part due to instrument limitations that have historically restricted field measurements to heights greater than roughly 10 cm from the bed, which is well outside the wave boundary layer (less than

1 cm for wind waves) and viscous and buffer layers associated with currents (also typically less than 1 cm in wave-dominated environments in estuaries).

In the past 10 years, computational fluid dynamics (CFD) has become a viable tool for investigating sediment dynamics in boundary layers. DNS was applied to study sediment transport in unidirectional (Cantero, Balachandar, Cantelli, et al., 2009; Cantero, Balachandar, & Parker, 2009; Yeh et al., 2013) and purely wave-driven (no currents) flows (Cheng et al., 2015; Ozdemir et al., 2010a; Yu et al., 2013). These studies focused on understanding the effects of sediment stratification on fluid dynamics. Cantero, Balachandar, Cantelli, et al. (2009) found that for unidirectional flow, sediment-induced stratification suppressed vertical momentum and mass transport, leading to a significant deviation from the expected logarithmic velocity profile. Bulk drag decreased with increasing sediment stratification, causing flow acceleration. Under strongly stratified conditions, turbulent channel flow can even laminarize, where turbulent shear stresses and sediment fluxes become negligible (Cantero, Balachandar, & Parker, 2009).

Wave simulations also indicate that sediment stratification can significantly impact flow structure. By varying sediment concentrations with fixed wave properties, Ozdemir et al. (2010a) found four regimes related to sediment transport in wave-driven flows. In order of increasing SSC, turbulence was either (1) uninhibited, (2) attenuated but only near the top of the boundary layer, (3) laminarized during portions of the wave cycle, or (4) laminarized during the entire wave cycle. Regime 2 has important implications for sediment transport because it lies between cases in which the water column is fully mixed and highly stratified. Cheng et al. (2015) built upon this work by including erosion and deposition in their simulations instead of prescribing a fixed sediment availability as did Ozdemir et al. (2010a). Their results confirm all but regime 3 and showed that for fixed wave properties, the transition between these regimes can be controlled by varying the critical shear stress for erosion. Yu et al. (2013) extended the work of Ozdemir et al. (2010a) by adding a linear non-Newtonian rheological model and comparing sediment-free to sediment-laden simulations with and without rheological affects. Viscosity increases were found to further attenuate flow by reducing near-bed velocity gradients and hence shear production.

The aforementioned studies confirm that CFD gives insight into sediment dynamics in unidirectional and purely wave-driven flows. A natural extension of this body of literature is to apply CFD to gain insight into fluid dynamics and sediment transport in the low wave Reynolds number regime typically found in estuaries. To this end, we present DNS of sediment dynamics in wave- and current-driven environments. We focus on conditions relevant to wind waves propagating onto shallow-water mudflats. The effects of waves on currents, and currents on waves, is presented in sections 3.1 and 3.2, respectively, while the remainder of the paper focuses on sediment dynamics. The role of currents on sediment mixing is discussed in section 3.3. We then examine the phase evolution of sediment entrainment and its connection to the bed shear stress (section 3.4.1), and how these variations affect near-bed SSC and sediment fluxes (section 3.4.2).

2. Problem Formulation

2.1. Problem Setup and Domain

When waves and currents coexist, the parameter space describing the fluid dynamics increases relative to the pure currents or pure waves cases, adding considerable complexity. Wave- and current-driven flows are uniquely characterized by five independent variables: (1) water depth H; (2) kinematic viscosity ν; (3) depth or volume-averaged current velocity $\overline{u}_c$; (4) bottom orbital velocity u_b; (5) and wave frequency $\omega = 2\pi/T$ (or wavelength via the dispersion relation), where T is the wave period. The Buckingham Pi theorem then implies that three nondimensional parameters completely specify the flow, which are often selected as the wave to current velocity ratio $\beta = u_b/\overline{u}_c$, the bulk Reynolds number $Re_B = \overline{u}_c H/\nu$, and the Stokes Reynolds number $Re_\Delta = u_b\Delta/\nu$, where $\Delta = \sqrt{2\nu/\omega}$ is the Stokes layer thickness. We note that the wave semiexcursion length can be selected instead of Δ, or the current friction velocity $u_* = (\langle\tilde{\tau}\rangle|_{z=0}/\rho)^{1/2}$ instead of $\overline{u}_c$, where ρ is the fluid density and $\langle\tilde{\tau}\rangle|_{z=0}$ is the time and planform-averaged bed shear stress. However, the resulting nondimensional parameters are similar.

Over decades of research on pulsating channel and pipe flows, many combinations of the dimensionless parameters have been explored and are summarized in the review articles by Gundogdu and Carpinlioglu (1999a, 1999b). However, surprisingly few investigations cover wave-dominated conditions in which $\beta = u_b/\overline{u}_c > 1$. The exception is the experimental work of Lodahl et al. (1998) and the numerical investigation of Manna et al. (2012, 2015), who examined pulsating pipe flows. This research gap is unfortunate given

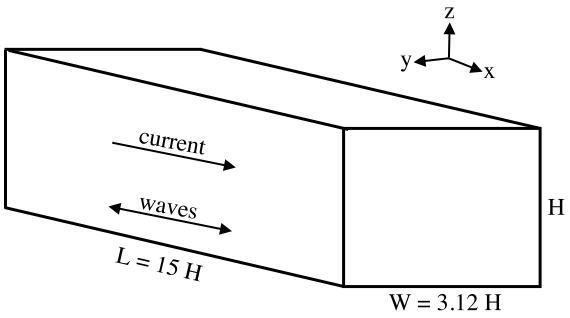

Figure 1. Three-dimensional representation of computational domain.

that wave-dominated conditions can occur in shallow-water estuarine environments during windy periods. Our work complements the wave-dominated literature by examining open channel flows (free-slip surface) instead of pipe flows, and we specifically focus on a parameter range relevant to wind waves and currents in shallow-water estuarine environments. We hold the bottom orbital velocity ($u_b = 10$ cm/s) and wave frequency ($\omega = 2\ s^{-1}$; $T = 3$ s; $\Delta \approx 1$ mm) constant, and vary mean currents between 0 and 9 cm/s. These wave and current properties are within the range observed in shallow-water regions of San Francisco Bay (Brand et al., 2010; Lacy et al., 2014; MacVean & Lacy, 2014). Although representative of field-scale conditions, the resulting Stokes Reynolds number $Re_\Delta = 100$ counterintuitively implies a laminar wave boundary layer (Hino et al., 1976). As will be shown, this has important implications for both flow and sediment dynamics.

We perform DNS of flow through a rectangular computational domain with streamwise, spanwise, and vertical dimensions of $15H \times 3.12H \times H$, where $H = 0.1$ m, that is discretized with $760 \times 320 \times 128$ cells (Figure 1). Flow boundary conditions are periodic in the horizontal, free slip at the top boundary ($\partial_z u = \partial_z v = 0$, $w = 0$), and no slip ($u = v = w = 0$) at the bottom boundary which we refer to as the bed. Grid spacing is constant in the horizontal, with $\Delta x = 2.0$ mm and $\Delta y = 0.98$ mm, or in wall units for the case with the strongest currents $\Delta x^+ = u_* \Delta x/\nu = 9.76$ and $\Delta y^+ = u_* \Delta y/\nu = 4.88$. In the vertical, 5% grid stretching is applied, with a minimum Δz at the bottom wall of 0.12 mm ($\Delta z^+ = u_* \Delta z/\nu = 0.60$; grid point nearest wall at $z^+ = 0.3$). Grid stretching ceases at a height in which $\Delta y = \Delta z$. From a grid resolution perspective, the viscous sublayer associated with the currents is the most challenging flow feature to resolve. For all conditions simulated, a minimum of 13 grid points were within $z^+ = 10$. As shown in section 2.5, this adequately resolves the viscous sublayer. Our grid resolution is finer than the DNS resolution applied and validated by Scotti and Piomelli (2001), and is comparable to that used by Manna et al. (2012). Following Moin and Kim (1982), two-point correlation functions were also computed to confirm that turbulent statistics are independent of the periodic boundary conditions.

2.2. Fluid Dynamic Solver

Flow is computed by solving the forced incompressible Navier-Stokes equation,

$$\frac{\partial u_i}{\partial t} + u_j \frac{\partial u_i}{\partial x_j} = -\frac{1}{\rho_0}\frac{\partial p}{\partial x_i} - g\delta_{i3} + \nu \frac{\partial^2 u_i}{\partial x_j^2} + S\delta_{i1}, \tag{1}$$

subject to continuity, $\partial_{xi} u_i = 0$, where p is the pressure, ν is the kinematic viscosity, S is a forcing term, δ_{ij} is the Kronecker delta, g is the gravitational acceleration, ρ_0 is the background density of water taken as 1,000 kg/m^3, ρ is the total density (defined in section 2.3), i and j take on values of 1, 2, and 3, corresponding to the x, y, and z directions, and the Einstein summation convention is assumed. We note that, since densimetric effects due to sediment are not included, the gravity term does not include density variability.

The forcing term is defined by a time invariant component, S_c, representing the mean pressure gradient driving currents, and an oscillating component, S_w, representing the wave pressure gradient,

$$S = S_c + S_w = \frac{u_*^2}{H} + u_b \omega \cos\theta\,, \tag{2}$$

where $\theta = \omega t$ is the wave phase. We note that S_w and the far-field wave velocity u_∞ (wave velocity where viscous effects are negligible) are out of phase by $\pi/2$. Modeling waves with an oscillating pressure gradient instead of resolving free-surface variations makes simulations computationally feasible and is commonly applied in CFD (Cheng et al., 2015; Ozdemir et al., 2010a, 2010b; Yu et al., 2013; Zedler & Street, 2006). This approach is valid when horizontal advection associated with the waves is small relative to unsteadiness (Nielsen, 1992), which is satisfied when $u_b k/\omega \ll 1$, where k is the wave number. Due to the rigid lid, there is no notion of a wave number arising from the dispersion relation, and hence, k is effectively infinite. However, in the presence of a surface wave with amplitude a_0 in water of depth D, $u_b k/\omega = (a_0/D)(kD/\sinh(kD)) \leq a_0/D$ since $kD/\sinh(kD) \leq 1$. Therefore, advection is generally weak relative to unsteadiness in typical estuarine environments given that $a_0 = O(0.1\text{ m})$ and $D = O(1\text{ m})$, implying $u_b k/\omega \leq a_0/D = O(0.1)$. Equation (1) is

solved with the incompressible flow solver originally developed by Zang et al. (1994) and later parallelized with MPI by Cui (1999). The flow solver was also applied to simulate sediment transport over bed forms in steady (Zedler & Street, 2001) and oscillating flows (Zedler & Street, 2006), and to study bed form evolution (Chou & Fringer, 2010). The governing equations are discretized using a finite-volume method on a nonstaggered grid in general curvilinear coordinates. All spatial derivatives are discretized using second-order central differencing with the exception of advection, where a variation of QUICK (quadratic upstream interpolation for convective kinematics) is employed (Leonard, 1979). Time advancement of diagonal viscous terms is performed with the second-order accurate Crank-Nicolson method, whereas all remaining terms are advanced in time with the second-order accurate Adams-Bashforth method. The fractional step projection method (Kim & Moin, 1985) is used to enforce a divergence-free velocity field.

The momentum equations are evolved with a time step size that ensures a maximum Courant number of 0.4. Simulations are run at the Army Research Laboratory DoD Supercomputing Resource Center on Excalibur (Cray XC40) using 480 processors per simulation. On average, simulation of one wave period requires 200 CPU hours or 25 min of wall clock time.

2.3. Suspended Sediment Transport

Suspended sediment transport is computed with the single-phase Eulerian approach, in which sediment is treated as a concentration by mass (kg/m^3) with the addition of a settling term, viz.

$$\frac{\partial C}{\partial t} + \frac{\partial}{\partial x_i}\left[C\left(u_i - \delta_{i3} w_s\right)\right] = K\frac{\partial^2 C}{\partial x_i^2}, \tag{3}$$

where C is the SSC, w_s is the settling velocity, and K is the effective sediment diffusivity. In the single-phase Eulerian approach, particle inertia, the volume occupied by the sediment, and momentum exchange between the sediment and fluid phase are ignored (Chou et al., 2014). These assumptions are valid when the volumetric sediment concentration (ratio of sediment volume to total volume) is less than 10^{-3}, and the Stokes number $St = \tau_p/\tau_\eta < 1$ (Balachandar & Eaton, 2010). Here $\tau_\eta = \sqrt{\nu/\epsilon}$ is the Kolmogorov time scale, and $\tau_p = \rho_s d^2/18\mu$ is the sediment or floc relaxation time scale, where d is the sediment or floc diameter, ρ_s is the sediment or floc density, μ is the dynamic viscosity of water, and ϵ is the turbulent dissipation rate. The parameter τ_p represents the time required to accelerate a sediment grain or floc from rest to the speed of the surrounding flow. Therefore, a small Stokes number implies that suspended sediment responds at a time scale shorter than the smallest time scales of the flow and hence can be treated as Lagrangian particles following the flow with the addition of a constant settling velocity.

In coastal regions and estuaries with fine sediment, both of the above conditions are often satisfied. As an example, Manning and Schoellhamer (2013) observed a median floc diameter and density of 200 μm and 1,888 kg m^3, respectively, in San Francisco Bay. At a nearby shallow-water site, MacVean and Lacy (2014) reported a turbulent dissipation rate of 10^{-4} m^2/s^3 and SSC up to 1,000 mg/L (high end of observed SSC) during moderate wave conditions. These measurements imply a Stokes number and volumetric sediment concentration of approximately 0.04 and 3×10^{-4}, respectively.

Sediment grains do not experience significant Brownian motion because of their relatively large size. However, slight variations in sediment properties (shape, density, and surface characteristics) and particle-particle interactions cause diffusion-like behavior of a sediment concentration field (Davis, 1996; Segre et al., 2001). The diffusion term in equation (3) accounts for these effects. For fine sediment, K is often approximated by assuming a Schmidt number $Sc = \nu/K \approx 1$ (Birman et al., 2005; Cantero, Balachandar, Cantelli, et al., 2009; Ozdemir et al., 2010a, 2010b; Necker et al., 2005). Following Ozdemir et al. (2010b), Birman et al. (2005), Cantero, Balachandar, Cantelli, et al. (2009), and Necker et al. (2005), we set $Sc = 1$. However, $0.5 \leq Sc \leq 2$ was tested. Schmidt number variations within this range only affect the magnitude of the SSC and do not influence our conclusions. Birman et al. (2005), Necker et al. (2005), and Bonometti and Balachandar (2008) all report similar insensitivity to Sc in turbulent flows.

Equation (3) is discretized with the finite-volume approach in the code of Zang et al. (1994). Spatial derivatives are approximated using second-order central differencing with the exception of advection, where Simple High-Accuracy Resolution Program is employed (Leonard, 1988). Time advancement of diagonal viscous terms is performed with the second-order accurate Crank-Nicolson method, whereas all remaining terms are time advanced with the second-order accurate Adams-Bashforth method. Periodic boundary conditions are applied to horizontal boundaries, and the no flux condition, $\left[K\partial_z C - \left(w - w_s\right)C\right]\Big|_{z=H} = 0$, is applied

at the top boundary. At the bed, sediment erosion (E) and deposition (D) are modeled with

$$E = -K\frac{\partial C}{\partial z}\bigg|_{z=0} = \begin{cases} M\left(|\tau|_{z=0}| - \tau_{\text{crit}}\right) & |\tau(z=0)| \geq \tau_{\text{crit}}\,, \\ 0 & \text{otherwise,} \end{cases} \tag{4}$$

and

$$D = -w_s C\big|_{z=0}\,, \tag{5}$$

where $\tau|_{z=0}$ is the bed shear stress computed as $\tau|_{z=0} = \mu\left(\partial_z u\big|_{z=0} + \partial_z v\big|_{z=0}\right)$, τ_{crit} is the critical shear stress of erosion (minimum shear stress required to mobilize sediment), and M is an empirical constant. We set $w_s = 5.8 \times 10^{-4}$ m/s and $\tau_{\text{crit}} = 0.1$ Pa. The settling velocity, critical shear stress, and form of the erosion rate model (equation (5)) are based on field observations of vertical cohesive sediment fluxes at a shallow-water site in South San Francisco Bay (Brand et al., 2015). In the environment, the settling velocities and bed properties (i.e., critical shear stress and erosion rate) for cohesive sediment are time variant due to flocculation (Hill et al., 2001) and bed consolidation (Parchure & Mehta, 1985; Sanford, 2008). However, we ignore these processes in the present work because they occur over time scales of O(1,000 s; Hill et al., 2001) for flocculation and days for consolidation (Sanford, 2008), whereas the sediment dynamics in this paper occur over time scales of O(1 s). The erosion model is also consistent with Type II erosion, which is typical under wave forcing (Sanford & Maa, 2001) and was applied by Cheng et al. (2015). The empirical constant $M = 0.01$ kg/s $\cdot$ m$^2\cdot$Pa was determined by adjusting M until the sediment concentration at the midchannel height was approximately 30 mg/L when $u_* = 0.005$ m/s and $u_b = 0.1$ m/s. This sediment concentration is within the range observed at shallow-water sites during conditions with comparable friction and bottom orbital velocities (Brand et al., 2010; Lacy et al., 2014; MacVean & Lacy, 2014). We note that past computational fluid dynamics simulations, with the exception of Cheng et al. (2015), assume equilibrium $E = D$ (Cantero, Balachandar, Cantelli, et al., 2009; Cantero, Balachandar, & Parker, 2009; Ozdemir et al., 2010a; Yu et al., 2013). However, the bed shear stress phase evolution resulting from waves causes an important imbalance between erosion and deposition, and hence assuming $E = D$ in our study would misrepresent near-bed sediment dynamics. Although sediment stratification affects the mixing of mass and momentum, it does not impact our conclusion related to sediment transport. We discuss the effects of sediment-induced stratification in a separate paper.

2.4. Notation and Terminology

In the analysis that follows, for an arbitrary variable ϕ at time step n, we represent discrete volume-averaging with an overbar $\overline{\phi}^n$, planform averaging with a tilde $\tilde{\phi}^n$, period averaging with angle brackets $\langle\phi\rangle$, and phase averaging with $\langle\phi\rangle_{\text{p}}$. Each is defined as

$$\overline{\phi}^n = \frac{1}{V}\sum_x\sum_y\sum_z \phi^n \Delta x \Delta y \Delta z\,, \tag{6}$$

$$\tilde{\phi}^n = \frac{1}{A}\sum_x\sum_y \phi^n \Delta x \Delta y\,, \tag{7}$$

$$\langle\phi\rangle = \frac{1}{N_T n_T}\sum_{j=1}^{N_T n_T} \phi^j\,, \tag{8}$$

and

$$\langle\phi\rangle_{\text{p}} = \frac{1}{N_T}\sum_{j=0}^{N_T-1} \phi^{j+P}\,, \tag{9}$$

where V is the domain volume, A is the planform area of the domain, N_T is the number of simulated wave periods, n_T is the number of time steps per wave period, and P is the wave phase being averaged over. Here x (or x_1), y (or x_2), and z (or x_3) are taken as the streamwise, spanwise, and vertical directions, respectively, and the superscripts indicate the time step. The corresponding streamwise, spanwise, and vertical velocity components are given by u (or u_1), v (or u_2), and w (or u_3). For current-only simulations, angle brackets imply time averaging over the entire simulation period.

We also decompose variables into a steady or current component ϕ_c, a wave component ϕ_w, and a fluctuating component ϕ', defined as

$$\phi_c = \langle\tilde{\phi}\rangle\,, \tag{10}$$

Table 1
Summary of Runs Performed

Run	Re_τ	Re_Δ	Re_B	$u_b/\bar{u}_c$	u_* (m/s)	u_b (m/s)	T (s)	Δ (mm)	N_T
200C	200	0	3168	n/a	0.002	0	n/a	n/a	150
200WC	200	100	3282	3.1	0.002	0.10	3	0.98	150
350C	350	0	6023	n/a	0.0035	0	n/a	n/a	150
350WC	350	100	6485	1.6	0.0035	0.10	3	0.98	150
500C	500	0	9039	n/a	0.005	0	n/a	n/a	150
500WC	500	100	9739	1.1	0.005	0.10	3	0.98	150
0W	0	100	0	0	0	0.10	3	0.98	150

$$\phi_w = \tilde{\phi} - \phi_c\,, \tag{11}$$

and

$$\phi' = \phi - \phi_c - \phi_w = \phi - \tilde{\phi}\,. \tag{12}$$

It then follows that ϕ can be written in decomposed form as

$$\phi^n = \phi_c + \phi_w^n + \phi'\,. \tag{13}$$

We note that $\langle\tilde{\phi}\rangle_p = \phi_c + \langle\phi_w\rangle$.

Variables are normalized by either *inner* or *outer* parameters depending on the comparison being made. Normalization by inner parameters is denoted by a superscript plus ($^+$), which implies wall units and nondimensionalization of length by the viscous length scale ν/u_*, and velocity by the current friction velocity u_*. For outer parameter scaling, length is nondimensionalized by the Stokes layer thickness Δ, and velocity by the bottom orbital velocity u_b. Lastly, we report SSC in milligrams per liter, which is typical for estuarine studies.

2.5. Test Cases

A total of seven simulations are run with the parameters summarized in Table 1. Simulations are labeled with the following nomenclature:

1. The leading number is a measure of the strength of the currents and indicates the friction Reynolds number $Re_\tau = u_* H/\nu$ associated with the time-invariant driving force (S_c) in the absence of waves.
2. The capital letters after the leading number indicate whether *currents alone* (C), *waves alone* (W), or *waves and currents* (WC) are simulated.

Current-only simulations (runs 200C, 350C, and 500C) are initialized with mean linear streamwise velocity profiles plus random perturbations drawn from a uniform distribution, and then time advanced while maintaining a constant flow rate as described by Nelson and Fringer (2017) until a linear total stress profile is obtained, and the volume-averaged turbulent kinetic energy ($\bar{k} = 0.5\overline{u_i' u_i'}$) is constant. Once both conditions are met, data are collected until turbulent statistics converge. In the absence of waves, no sediment is suspended because the bed shear stress for current-only runs does not exceed the critical shear stress for erosion.

Recall that the wave strength is constant for all simulations including waves, with $T = 3$ s and $u_b = 0.10$ m/s. Wave and current simulations (runs 200WC, 350WC, and 500WC) are initialized with the flow field from the corresponding current-only runs and time advanced for 170 wave periods. At this point the running average of $\langle\bar{C}\rangle$ changes by less than 0.01%. We note that the spinup time is roughly a factor of 3 longer than the settling time scale $H/w_s = 174$ s (58 wave periods), which is the longest time scale affecting SSC. Data recording begins after 170 wave periods, and simulations are continued until phase- and period-averaged turbulent statistics for both the flow field and sediment field converge. We note that the mean pressure gradient is held constant between paired current-only and wave and current runs (e.g., between 200C and 200WC) to explicitly examine flow acceleration due to the waves given the same driving pressure gradient. The current-only and wave-only runs serve as baseline conditions for comparison to the combined wave current cases.

To validate the model, planform- and time-averaged streamwise velocity profiles ($u_c^+ = u_c/u_*$) for current-only runs are shown in Figure 2. The theoretical log law $u_{log}/u_* = 1/\kappa \ln(z/z_0)$ is also plotted for comparison, where $\kappa = 0.41$ is the von Kármán constant and $z_0 = \nu/(9u_*)$ is the smooth-wall bed roughness (viscous sublayer is included to $z^+ = 11.6$). All runs clearly show a viscous sublayer (approximately $0 \le z^+ \le 5$), buffer layer

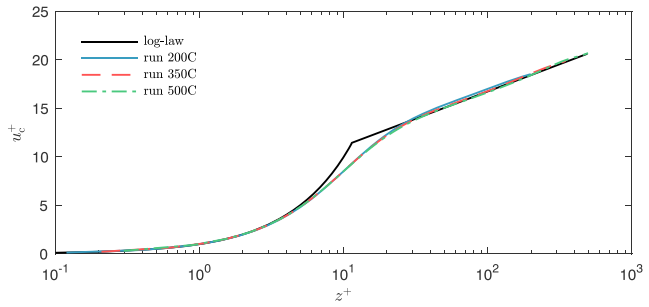

Figure 2. Time- and planar-averaged velocity ($u_c^+ = u_c/u_*$) profiles for current-only runs with Re_τ of 200 (run SC200), 350 (run SC350), and 500 (run SC500). For comparison, the theoretical log law is included.

(approximately $5 < z^+ \leq 30$), and log layer (approximately $z^+ > 30$), with the transition between regions at the expected heights (Pope, 2000). The slight deviation between the simulations and log law near the top of the water column is caused by the well-documented wake region (Pope, 2000). We also note that the overshoot for run 200C is consistent with past DNS simulations of low Reynolds number turbulent channel flow and is vertically indistinguishable from results reported by del Alamo et al. (2004).

3. Results and Discussion

3.1. Effects of Waves on Currents

Vertical profiles of planform- and period-averaged streamwise currents ($u_c^+ = u_c/u_*$) are plotted in Figure 3 for runs 200WC, 350WC, and 500WC. The theoretical log law is again included for comparison. Current velocity profiles for all wave and current simulations contain a clear viscous sublayer, buffer layer, and log layer. The general shape of each profile resembles the corresponding current-only runs plotted in Figure 2. However, the waves act to thicken the viscous sublayer, reduce the net drag on the flow, and increase current magnitudes (upward shift in velocity profiles). Similar increases in current magnitude for pulse-dominated pipe flows are reported in both experimental (Lodahl et al., 1998) and numerical (Manna et al., 2012, 2015) investigations.

A thicker viscous sublayer indicates reduced vertical turbulent momentum transport to the near-bed region. Less low-momentum fluid near the bed is mixing with the overlying high momentum fluid. The effect of waves on currents is seen in the expression for u_c, which is found by first substituting $u = u_c + u_w + u'$ into equation (1), and planform- and period-averaging to give

$$\nu \frac{d^2 u_c}{dz^2} = \frac{d}{dz}\left[\left(\widetilde{u'w'}\right)_c\right] - \frac{u_*^2}{H}, \tag{14}$$

Because the bed is impermeable, $\left(\widetilde{u'w'}\right)_c|_{z=0} = 0$, and equation (15) at the bed reduces to $\partial_z u_c|_{z=0} = u_*^2/\nu$, or $\mu \partial_z u_c|_{z=0} = \rho_0 u_*^2$. This implies that the bed shear stress andwhere we have made the substitution $S_c = \frac{u_*^2}{H}$. Equation (14) was simplified by recognizing that wave and current velocity components pass through planform-averaging, $\widetilde{u'}_i = 0$, and $\langle S_w \rangle = 0$. Integrating equation (14) and applying the free-slip condition at $z = H$ then gives

$$\frac{du_c}{dz} = \frac{1}{\nu}\left[\left(\widetilde{u'w'}\right)_c + u_*^2\left(1 - \frac{z}{H}\right)\right]. \tag{15}$$

friction velocity associated with the mean currents do not change in the presence of waves, and hence, $u_* = (\langle \tilde{\tau} \rangle|_{z=0}/\rho)^{1/2} = (HS_c/\rho)^{1/2}$. Equation (15) can be further integrated and rearranged to give the steady current velocity profile (now with $S_c = \frac{u_*^2}{H}$)

$$u_c(z) = \frac{1}{\nu}\left[S_c z\left(H - \frac{1}{2}z\right) + \int_0^z \left(\widetilde{u'w'}\right)_c dz\right]. \tag{16}$$

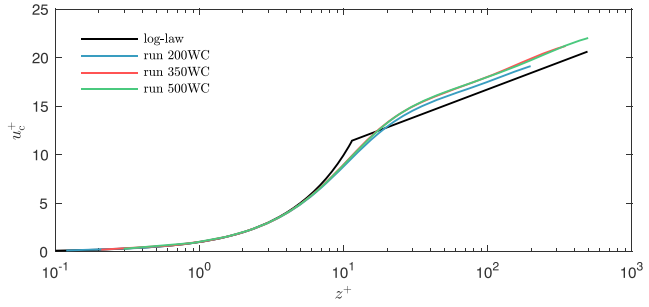

Figure 3. Period- and planar-averaged velocity profiles for wave and current runs 200WC, 350WC, and 500WC. For comparison, the theoretical log low is included.

Equation (16) indicates that the magnitude of the streamwise current is determined by the strength of the mean driving force or pressure gradient, S_c, and the vertically integrated planform- and period-averaged vertical Reynolds stress $(\widetilde{u'w'})_c$. This shows that waves affect the mean currents by modifying the vertical Reynolds stress, even though the bottom stress is not affected.

Profiles of planform- and period-averaged vertical Reynolds stress $-(\widetilde{u'w'})_c^+$, mean current shear stress $\partial_z u_c^+$, and total stress $\tilde{\tau}^+ = \partial_z u_c^+ - (\widetilde{u'w'})_c^+$ for current-only and wave and current runs are plotted in Figure 4. From equation (14), the total stress is given by $\tilde{\tau}^+ = (1 - z/H)$, behavior that

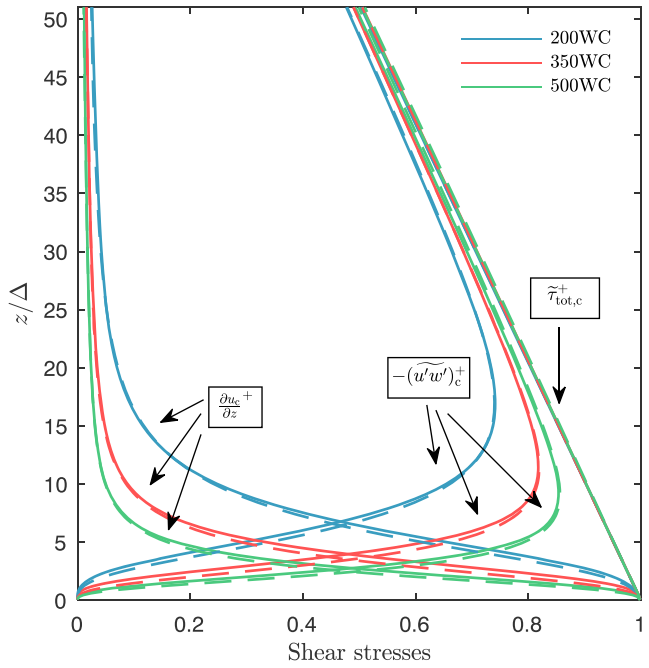

Figure 4. Period- and planform-averaged viscous $\frac{\partial u_{\mathrm{c}}}{\partial z}^{+}$, turbulent $-(\widetilde{u'w'})^{+}_{\mathrm{c}}$, and total stresses $\tau^{+}_{\mathrm{tot,c}}$ profiles. The solid lines correspond to wave and current simulations (200WC, 350WC, and 500WC), whereas the dashed lines are the current-only runs (200C, 350Ca, and 500C). Line coloring is based on the current magnitude (e.g., 200C and 200WC are both blue). Profiles are plotted from the bed to the midchannel height.

is confirmed in the simulations. Reynolds stress magnitudes increase and peak closer to the bed with increasing Re_{τ} for both wave and current, and current-only runs. This behavior is well documented for current-only turbulent channel flow (Lee & Moser, 2015; Schultz & Flack, 2013). Interestingly, for the conditions simulated, waves decrease the Reynolds stress magnitudes and slightly shift the peaks higher into the water column. Decreased magnitudes of $-(\widetilde{u'w'})^{+}_{\mathrm{c}}$, and hence decreased vertical momentum transport, indicate the integration in equation (16) is a smaller negative number relative to the corresponding current-only run. As a result, u_{c} increases. The experimental data of Lodahl et al. (1998) and the numerical results of Manna et al. (2012) suggest that the transition from turbulent to laminar flow conditions is delayed for weak currents in the presence of laminar waves with large bottom orbital velocities. However, our results indicate that, for the conditions simulated, stronger currents are accelerated more than weaker currents by laminar waves (Figure 3). The effect of waves on the Reynolds stress is also more pronounced for stronger currents (Figure 4). All stress profiles resulting from wave and current runs approach their corresponding current-only profiles as z increases.

Reduced turbulent vertical momentum transport to the near-bed region is manifested as a smaller drag coefficient defined as $C_D = u_*^2/\overline{u}_{\mathrm{c}}^2$. In the presence of waves, C_D is reduced by as much as 13% (runs 350WC and 500WC in Table 2). Similarly, the bottom roughness, z_0, calculated by solving $C_{\mathrm{D}} = \left(1/\kappa\left[\ln(H/z_0) + z_0/H - 1\right]\right)^{-2}$, decreased by roughly 39% for runs 350WC and 500WC. Drag coefficients and bottom roughness ratios are shown in Table 2. We note that in the presence of sediment-induced stratification, currents are further accelerated and the effects are more pronounced for weaker currents. Stratification effects will be reported in a separate paper.

When both the current boundary layer and wave boundary layer are turbulent, due to large bed roughness or higher Reynolds number waves, the effect of the wave boundary layer on the overlaying current boundary layer is an enhanced roughness (Grant & Madsen, 1979). However, the results presented in Table 2 suggest that in fine sediment environments with low Reynolds number waves, the resulting laminar wave boundary layer acts to reduce the bottom roughness and drag. This implies that wave and current boundary layer models that assume a fully turbulent wave boundary layer and a hydraulically rough bottom are not always applicable for estuarine conditions.

For comparison, we fit our simulation results to the wave and current boundary layer model developed by Styles et al. (2017), which is a variant of the model of Grant and Madsen (1979) in that Styles et al. (2017) assume a three-layer rather than two-layer eddy viscosity model. The model of Styles et al. (2017) is employed in the commonly used Regional Ocean Modeling System (Warner et al., 2008) to specify the bottom stress in combined wave and current conditions. The model requires a mean velocity specified at a reference height, which we assume is $z = H/4$, a median grain or floc diameter for the sediment bed, a bottom orbital velocity, a wave semiexcursion length, and the angle between the waves and currents. We assign a medium floc diameter of 100 μm based on the sediment bed grab samples reported by Jones and Jaffe (2013) for a shallow-water wavy

Table 2
Ratios of Bed Roughness and Drag Coefficients for Runs With (WC Subscript) and Without Waves (C Subscript), and Ratios of Simulated Wave and Current Drag Coefficients, Bottom Roughness, and Current Friction Velocities to Predicted Values From the Wave and Current Boundary Layer Model of Styles et al. (2017) (Indicated by S2017 Subscript)

Run	$C_{D,\mathrm{WC}}/C_{D,\mathrm{C}}$	$C_{D,\mathrm{WC}}/C_{D,\mathrm{S2017}}$	$z_{0,\mathrm{WC}}/z_{0,\mathrm{C}}$	$z_{0,\mathrm{WC}}/z_{0,\mathrm{S2017}}$	$u_{*,\mathrm{WC}}/u_{*,\mathrm{S2017}}$
200WC	0.94	0.63	0.82	0.25	0.79
350WC	0.87	0.69	0.61	0.27	0.82
500WC	0.87	0.74	0.61	0.33	0.86

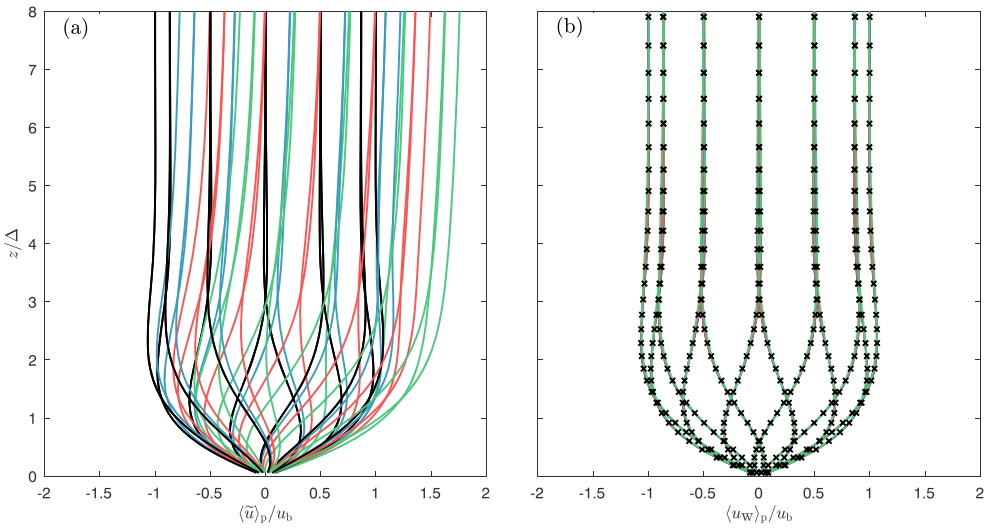

Figure 5. Vertical profiles of (a) planform- and phased-averaged velocity $\langle\tilde{u}\rangle_p$ and (b) the phased-averaged wave-induced velocity $\langle u_w\rangle_p$. The black crosses in panel (b) represent Stokes solution, which is essentially identical to $\langle u_w\rangle_p$ for all runs. Line colors for the wave and current runs follow Figure 3, and the black lines correspond to run 0W.

site in South San Francisco Bay. Ratios of simulated to model-predicted drag coefficients, bottom roughness, and current friction velocities are shown in Table 2. For the conditions simulated, the model of Styles et al. (2017) overpredicts the drag coefficient and associated bottom roughness and friction velocities.

3.2. Effects of Currents on Waves

The effects of currents on waves is examined by deriving the governing equation for $\langle u_w\rangle_p$. We begin by planform averaging the Navier-Stokes equation (equation (1)) to give

$$\frac{\partial u_w}{\partial t}+\frac{\partial}{\partial z}\left[\left(\widetilde{u'w'}\right)_c+\left(\widetilde{u'w'}\right)_w\right]=\nu\frac{\partial^2}{\partial z^2}\left(u_c+u_w\right)+S_c+S_w\,, \tag{17}$$

where $u_c+u_w=\tilde{u}$ and $(\widetilde{u'w'})_c+(\widetilde{u'w'})_w=\widetilde{u'w'}$. Applying equation (14), current terms cancel, and after phase averaging, equation (17) can be simplified to give

$$\frac{\partial}{\partial t}\left(\langle u_w\rangle_p\right)+\frac{\partial}{\partial z}\left(\langle(\widetilde{u'w'})_w\rangle_p\right)=\nu\frac{\partial^2}{\partial z^2}\left(\langle u_w\rangle_p\right)+S_w\,. \tag{18}$$

Equation (18) indicates that currents can only affect waves by modifying the wave component of the Reynolds stress $\langle(\widetilde{u'w'})_w\rangle_p$. However, for the wave and current conditions tested, gradients in the Reynolds stress are negligible within the wave boundary layer, and thus equation (18) can be analytically solved following the solution procedure for Stokes second problem (Nielsen, 1992), to give

$$u_{\text{Stokes}}\left(z,t\right)=u_b\left[\cos\left(\omega t\right)-\exp\left(-\frac{z}{\Delta}\right)\cos\left(\omega t-\frac{z}{\Delta}\right)\right]\,. \tag{19}$$

Because the Reynolds stress term is negligible in the wave boundary layer, currents do not significantly affect the wave velocity for the conditions tested. Planform- and phased-averaged velocity profiles ($\langle\tilde{u}\rangle_p=u_c+\langle u_w\rangle_p$) are plotted for different phases of the wave cycle for runs 0W, 200WC, 350WC, and 500WC in Figure 5a. Comparing the wave-only to the combined wave and current runs, profiles are shifted in the direction of the mean flow by an amount that increases as the strength of the currents increases. However, after decomposing the velocity field, the wave velocity for all runs and phases is nearly indistinguishable from Stokes solution (Figure 5b), confirming nearly complete decoupling of waves from currents.

Similar decoupling of the oscillating and steady mean currents for pulsating flows with normalized forcing frequencies $\omega^+=\omega\nu/u_*^2$ similar to the conditions tested ($0.08<\omega^+<0.5$) were reported for channel (Scotti & Piomelli, 2001; $\omega^+=0.1$) and pipe (Manna et al., 2012; $\omega^+=0.22$ and 0.48) flows. Within this range of ω^+ values, the wave boundary layer is smaller than the viscous sublayer thickness, where turbulence is weak

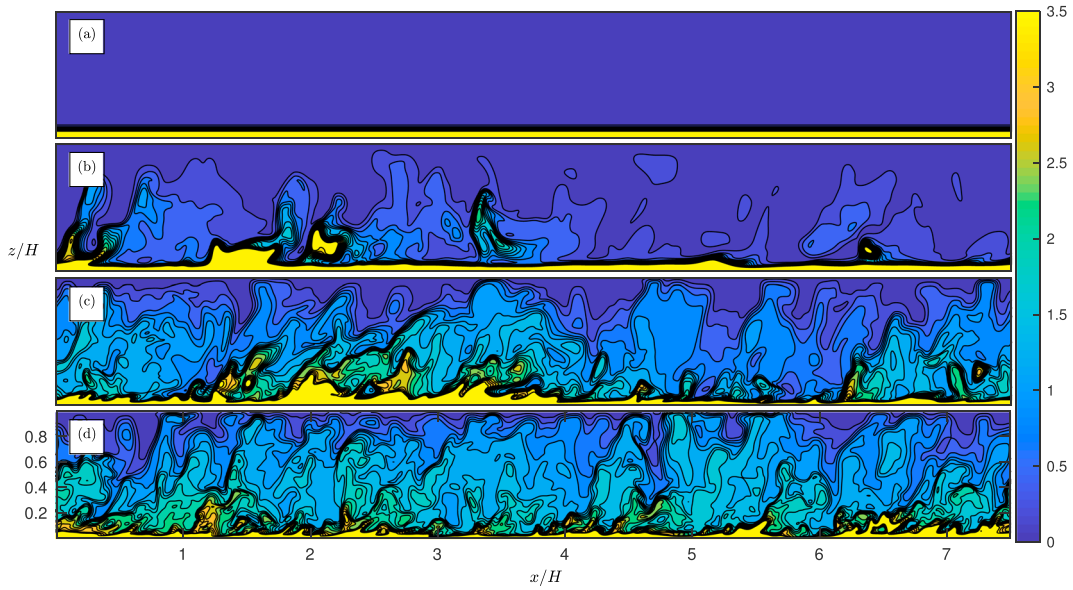

Figure 6. Contours of instantaneous suspended sediment concentration normalized by $\langle \overline{C} \rangle$ along the channel centerline for runs (a) 0W, (b) 200WC, (c) 300WC, and (d) 500WC at $\theta = 4\pi/3$.

and does not significantly impact vertical turbulent mixing. For run 500WC, which has the strongest currents and hence the smallest viscous sublayer thickness, the peak wave velocity occurs at approximately $z^+ = 10$ ($z = 2\Delta$) and hence is in the transition region between the viscous sublayer and buffer layer. The slight increase in $\langle u_w \rangle_p$ for run 500WC from $3 < z/\Delta < 6$ likely occurs because the wave boundary layer extends slightly past the viscous sublayer.

3.3. Effect of Currents on SSC

The oscillatory nature of waves causes the near-bed SSC to vary significantly throughout the wave cycle. However, above the wave boundary layer, phase variations in SSC are negligible. Above $z = 5\Delta$, planform- and phased-averaged SSC for all conditions tested is within 2% of the period-averaged SSC throughout the wave cycle. The phase independence of the SSC indicates that currents control vertical sediment mixing outside of the wave boundary layer. To visualize the role of currents on sediment transport, instantaneous sediment concentrations normalized by $\langle \overline{C} \rangle$ are contoured over a vertical streamwise plane in Figure 6.

In the absence of currents (Figure 6a), the bed shear stress from waves alone exceeds the critical shear stress during a portion of the wave cycle. However, the sediment remains within the wave boundary layer because vertical mixing is negligible. As will be discussed in section 3.4.1, adding weak currents (run 200WC) does not significantly increase the net sediment entrainment rate from the bed, although it generates turbulence in the near-bed region that transports sediment into the overlying water column (Figure 6b). SSC increases substantially above the viscous sublayer (roughly 5Δ for 200WC) relative to the wave-only run. Increasing the current magnitude further increases the amount of sediment transported up into the water column (Figures 6c and 6d). We note that in the absence of waves, current-only runs do not exceed the critical shear stress and hence sediment is not suspended.

The sediment flux budget for the current component of the SSC is derived by first planform- and period-averaging equation (3)

$$\frac{\partial}{\partial z}\left[\left(\widetilde{w'c'}\right)_c\right] - \frac{\partial}{\partial z}\left[w_s C_c\right] = K\frac{\partial^2 C_c}{\partial z^2}, \tag{20}$$

then vertically integrating to give

$$\left(\widetilde{w'c'}\right)_c - w_s C_c - K\frac{\partial C_c}{\partial z} = F_{T,c} + F_{s,c} + F_{D,c} = 0, \tag{21}$$

where $F_{T,c} = (\widetilde{w'c'})_c$, $F_{s,c} = -w_s C_c$, and $F_{D,c} = -K\partial_z C_c$ are the current components of the turbulent, settling, and diffusive sediment fluxes, respectively, and we assume no net sediment flux at the free surface.

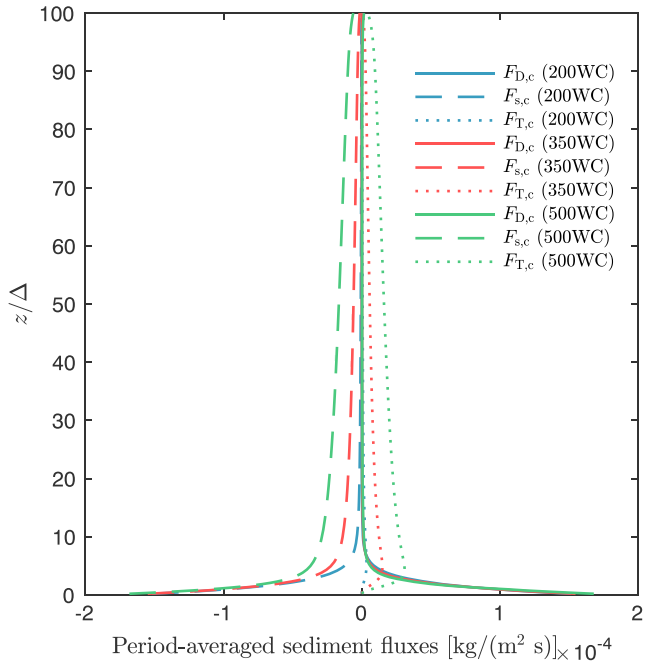

Figure 7. Vertical profiles for the sediment transport budget governing the time-averaged suspended sediment concentration. Runs 200WC, 350WC, and 500WC are plotted. Line type indicates the flux type, and line color indicates the run.

Sediment flux profiles are shown in Figure 7 for all wave and current runs. The shape of the sediment flux profiles is similar between runs, but flux magnitudes increase with increasing currents. In the near-bed region, the downward settling flux predominately balances the upward diffusive flux for all runs. However, within the buffer layer, vertical turbulent sediment fluxes increase and become larger than the diffusive flux at roughly $z^+ = 13$. In terms of absolute height above the bed, vertical turbulent sediment fluxes become important closer to the bed as currents increase because the viscous sublayer is thinner for stronger currents.

The downward settling flux balances the upward vertical turbulent flux throughout most of the water column, with both fluxes decreasing with height above the bed as turbulence weakens and sediment concentrations decrease. In the absence of waves, this balance leads to the theoretical Rouse profile

$$C_{\mathrm{Rouse}} = C_a \left(\frac{H-z}{z} \frac{a}{H-a} \right)^{Ro}, \tag{22}$$

where C_a is the sediment concentration at reference height a, and $Ro = Sc\, w_s/(\kappa u_*)$ is the Rouse number. If C_a is taken as C_c at the top of the buffer layer ($z^+ = 30$) where turbulent fluxes are approximately 10 times larger than the diffusion flux, the corresponding analytical Rouse profile, with the friction velocity defined by $u_* = (\langle \tilde{\tau} \rangle|_{z=0}/\rho)^{1/2}$, closely resembles C_c profiles for all combined wave- and current-driven runs (Figure 8). The profile fits are somewhat surprising considering the Rouse profile is derived by assuming unidirectional, statistically steady flow with a parabolic eddy-viscosity profile and $E = D$. However, the wave period (3 s) is much less than the settling time scale H/w_s (173 s) of the water column, so sediment concentrations cannot rapidly respond to changes in sediment entrainment rates throughout most of the water column. Therefore, sediment dynamics above the buffer layer closely resemble that of purely current-driven flow.

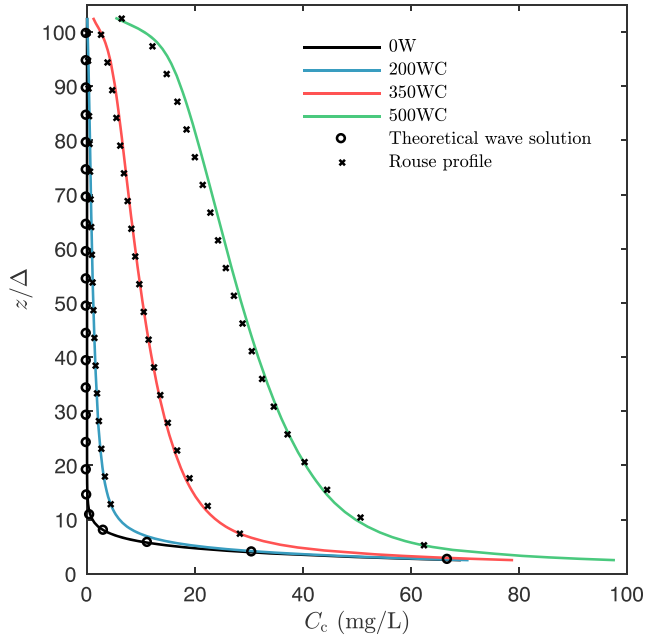

Figure 8. Period- and planform-averaged sediment concentration C_c profiles for runs 200WC, 300WC, and 500WC. The black circles represent the theoretical period-averaged sediment profile for laminar, purely wave-driven flows, and the black crosses represent the theoretical Rouse profile computed with C_a taken as C_c at the top of the buffer layer ($z^+ = 30$) and the friction velocity defined by $u_* = (\langle \tilde{\tau} \rangle|_{z=0}/\rho)^{1/2}$.

Table 3
Ratio of SSC and the Total Vertical Sediment Flux at the Bed and the Top of the Buffer Layer

Run	200WC	350WC	500WC
$\frac{C_c(z^+=0)}{C_c(z^+=30)}$	82.3	11.4	5.5
$\frac{F_{vert}(z^+=0)}{F_{vert}(z^+=30)}$	81.9	11.3	5.6

Note. SSC = suspended sediment concentration.

Comparing the wave-only run (run 0W) to the run with waves and weak currents (run 200WC) again shows that waves generate high SSC near the bed, but currents control mixing throughout most of the water column. Up to $z \approx 6\Delta$), the two profiles are virtually indistinguishable and match the theoretical period-averaged sediment profile for a laminar, purely wave-driven flow, $\langle\tilde{C}\rangle = \langle\tilde{C}\rangle|_{z=0}\exp(-w_s z/K)$. However, at roughly $z = 6\Delta$, the buffer layer begins for run 200WC, and vertical turbulent sediment fluxes become import. Turbulence vertically transports sediment and significantly increases the sediment concentration for run 200WC relative to run 0W. In the absence of currents, suspended sediment concentrations are negligible above $z = 10\Delta$.

We note that when modeling fluid dynamics and sediment transport on scales relevant to estuarine management [O(1 km) to O(100 km)], computational restrictions require the use of turbulent closures and wall models. In these applications, sediment fluxes across the bottom boundary of the domain represent the vertical turbulent sediment flux at the bottom of the log law (e.g., top of the buffer layer). Physical processes occurring within the wave boundary layer, viscous sublayer, and buffer layer are not resolved and are instead parameterized by the erosion model. We briefly examine the connection between the total planform- and period-averaged vertical sediment fluxes ($F_{vert,c} = F_{D,c} + F_{T,c}$) at the bed and the top of the buffer layer. At the bed, $\langle\tilde{E}\rangle = F_{D,c} = C_c w_s$ when C_c is statistically steady. We note that because the wave velocity is decoupled from the current velocity for the conditions tested, $\langle\tilde{E}\rangle$ can be analytically computed by period averaging E defined by equation (4) with $\tau = \rho u_*^2 + \tau_{Stokes}$, where $\tau_{Stokes} = \mu u_b/\Delta\,(\cos(\omega t - z/\Delta) - \sin(\omega t - z/\Delta))$ is the bed shear stress from Stokes solution. Analytical calculations of $\langle\tilde{E}\rangle$ are virtually identical to the model results.

Ratios of C_c and the vertical sediment flux at the bed and the top of the buffer layer are shown in Table 3. The difference between the sediment concentration and vertical sediment fluxes decreases with increased currents, because the top of the buffer layer is closer to the bed, and vertical turbulent fluxes are larger for stronger currents. The amount of sediment mixed into the water column is dependent on the distance between the wave boundary layer and buffer layer. The difference between $F_{vert,c}$ at the bed and the top of the buffer layer illustrates that the prescribed vertical sediment flux in simulations with a resolved boundary layer do not match the necessary boundary conditions for simulations employing wall models. To the best of our knowledge, no universal erosion model is reported in the literature that is applicable to both resolved and unresolved simulations. Developing such a relationship is critical for connecting boundary layer dynamics derived from CFD results to field-scale parameterizations.

3.4. Effect of Waves on SSC

3.4.1. Bed Shear Stress and Entrainment

Currents dominate sediment transport throughout most of the water column, but the high bed shear stress resulting from waves controls the total amount of suspended sediment by governing the sediment entrainment rate. Phase variations in the volume-averaged SSC and its dependence on the sediment entrainment rate are seen by volume averaging equation (3), which gives

$$\begin{aligned}\frac{d\overline{C}}{dt} &= \frac{1}{V}\sum_x\sum_y\sum_z\left\{K\frac{\partial^2 C}{\partial x_i^2} - \frac{\partial}{\partial x_i}\left[C\left(u_i - \delta_{i,3}w_s\right)\right]\right\},\\ &= \frac{1}{V}\sum_x\sum_y\left\{K\frac{\partial C}{\partial x_i} - C\left(w - w_s\right)\right\}_T\\ &\quad - \frac{1}{V}\sum_x\sum_y\left\{K\frac{\partial C}{\partial x_i} - w_s C\right\}_B,\end{aligned} \tag{23}$$

where T and B subscripts correspond to the top (lid) and bottom (bed) boundaries, respectively. We move from the volume to the surface integration in equation (23) by applying the discrete form of Gauss's theorem, and terms containing fluxes evaluated at sidewalls are eliminated due to horizontal periodicity. Assuming no sediment flux through the surface and applying the sediment boundary conditions at the bed (equation (4)) gives

$$\frac{d\overline{C}}{dt} = \frac{1}{V}\sum_x\sum_y(E - D) = \frac{1}{H}\left(\tilde{E} - \tilde{D}\right) = \frac{1}{H}\tilde{E}_{net}, \tag{24}$$

where $\tilde{E}_{net} = \tilde{E} - \tilde{D}$ is the net sediment entrainment rate. When $\tilde{E}_{net} > 0$, the total amount of sediment in the water column increases with time.

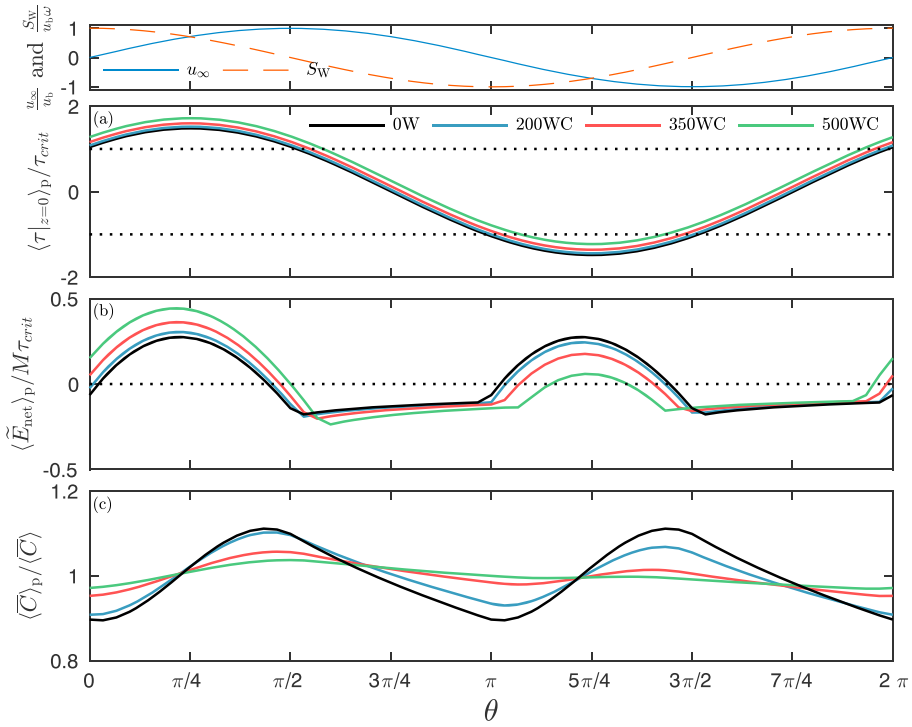

Figure 9. The planform- and phased-averaged (a) bed stress $\langle\tilde{\tau}\rangle_p|_{z=0}$ and (b) net sediment entrainment $\langle E_{net}\rangle_p$, and (c) planform- and phased-averaged suspended sediment concentration $\langle\overline{C}\rangle_p$ for runs 0W, 200WC, 350WC, and 500WC. The black dotted lines in (c) indicate $\pm\tau_{crit}$ and $\langle\tilde{\tau}\rangle_p|_{z=0} = 0$. The far-field wave velocity and wave pressure gradient are plotted in the top panel for reference.

To assess the phase evolution of the total amount of suspended sediment and its connection to the bed shear stress and sediment entrainment rate, $\langle\overline{C}\rangle_p$, $\langle\tilde{\tau}\rangle_p|_{z=0}$, and $\langle\tilde{E}_{net}\rangle_p$ are plotted in Figure 9. We start by describing features of the bed shear stress (Figure 9a). $|\langle\tilde{\tau}\rangle_p|_{z=0}| > \tau_{crit}$ implies erosion is generally occurring. The bed shear stress leads the far-field wave velocity by $\pi/4$, and is indistinguishable from Stokes solution for run 0W. For all runs, the bed shear stress peaks at $\theta = \pi/4$ and $5\pi/4$. Although currents do not alter the phase of the bed shear stress, they increase $\langle\tilde{\tau}\rangle_p|_{z=0}$ by an amount $\rho_0 u_*^2$. Thus, runs with stronger currents have larger maximum bed stresses, leading to changes in the timing and rate of sediment entrainment. Generally, stronger currents increase the duration in which the bed shear stress exceeds the critical shear stress when the wave pressure gradient drives flow in the direction of the currents. We will refer to this as a *favorable* wave pressure gradient corresponding to the phases $0 \leq \theta \leq \pi/2$ and $3\pi/2 \leq \theta \leq 2\pi$. The bed shear stress for run 500WC is the first to exceed and last to fall below the critical shear stress. The opposite is true when the wave pressure gradient opposes the currents, which we will refer to as an *adverse* wave pressure gradient ($\pi/2 < \theta < 3\pi/2$). When the wave pressure gradient is adverse, stronger currents decrease the duration in which the bed shear stress is larger than the critical shear stress. Run 500WC is the last to exceed and first to fall below τ_{crit} when the wave pressure gradient is adverse.

The increase in the bed shear stress resulting from currents also causes an asymmetry in sediment entrainment rates and volume-averaged SSC. In the absence of currents (run 0W), $\langle\tilde{E}_{net}\rangle_p$ and $\langle\overline{C}\rangle_p$ peak twice per period with the identical magnitude at each peak (Figures 9b and 9c). However, adding currents increases sediment entrainment rates when the wave pressure gradient is favorable because the difference between the bed shear stress and the critical shear stress is larger. The converse is true when the wave pressure gradient is adverse. $\langle\tilde{E}_{net}\rangle_p$ and $\langle\overline{C}\rangle_p$ still peaks twice per wave period, but sediment entrainment during the adverse pressure gradient is smaller when currents are larger. Paradoxically, near-bed SSC can be smaller when the currents are stronger (see section 3.4.2).

Phase variations in the bed shear stress cause several distinct characteristics in the net sediment entrainment rate. When the shear stress exceeds the critical shear stress, sediment entrainment generally increases with increasing bed shear stress (roughly $0 < \theta < \pi/4$ and $\pi < \theta < 5\pi/4$). However, the sediment entrainment

rate peaks slightly before the bed shear stress. When $\langle\tilde{\tau}\rangle_p|_{z=0}$ is rapidly increasing in time, erosion increases faster than deposition, and the net sediment entrainment rate and volume-averaged SSC increase. However, as the time rate of change of $\langle\tilde{\tau}\rangle_p|_{z=0}$ decreases, the near-bed sediment concentration quickly adjusts within the wave boundary layer because both the sediment diffusion Δ^2/K and settling time scale (Δ/w_s) associated with the wave boundary layer are less than the wave period. As the magnitude of the bed shear stress decreases between roughly $\pi/4 < \theta < \pi/2$ and $5\pi/4 < \theta < 3\pi/2$, the erosion rate decreases faster than the deposition rate. $\langle\tilde{E}_{net}\rangle_p$ drops below zero at $\theta \approx \pi/2$ and $3\pi/2$, implying the volume-averaged SSC is decreasing.

When the magnitude of the bed shear stress falls below the critical shear stress, erosion is eliminated, although the depositional flux also decreases because near-bed SSC decreases and hence less sediment is available for deposition. Without erosion, the volume-averaged sediment concentration exponentially decays (roughly $\pi/2 < \theta < \pi$ and $3\pi/2 < \theta < 2\pi$). If erosion was eliminated for a time period longer than the settling time scale of the water column (H/w_s), nearly all sediment would deposit and the net sediment entrainment rate and volume-averaged sediment concentration would vanish.

We emphasize that the phase evolution of $\langle\tilde{E}_{net}\rangle_p$ and $\langle\tilde{C}\rangle_p$ can only be assessed in oscillating flows if erosion and deposition are explicitly modeled. Therefore, applying the commonly used boundary condition $E = D$ (Cantero, Balachandar, Cantelli, et al., 2009; Cantero, Balachandar, & Parker, 2009; Ozdemir et al., 2010a; Yu et al., 2013) would not accurately capture the time variability of the sediment dynamics in wave- and current-driven flows.

Although waves cause phase variations in sediment entrainment rates and near-bed SSC, the variations do not significantly impact the net streamwise sediment transport. This is seen by calculating the net depth-integrated and period-averaged flux (which is also planform averaged). Recognizing that u_c, u_w, C_c, and C_w pass through planform averaging, and $\widetilde{u'} = \widetilde{C'} = \langle u_w\rangle = \langle C_w\rangle = 0$, the net sediment flux is given by

$$F = \langle \int_0^H \widetilde{uC}\,dz\rangle = F_c + F_w + F', \tag{25}$$

where the current-driven flux is

$$F_c = \int_0^H \widetilde{u_c C_c}\,dz, \tag{26}$$

the wave-driven flux is

$$F_w = \int_0^H \langle\widetilde{u_w C_w}\rangle\,dz, \tag{27}$$

and the turbulent flux is

$$F' = \int_0^H \langle\widetilde{u'C'}\rangle\,dz. \tag{28}$$

Our simulations indicate that the net streamwise turbulent flux, F', is negligible, implying that the primary contributors to the net streamwise flux are the current- and wave-driven components F_c and F_w. However, ratios of the wave- to current-driven fluxes are small and are given by $F_w/F_c = 0.02$, 0.005, and 0.003 for runs 200WC, 350WC, and 500WC, respectively, implying that the asymmetric entrainment has a relatively small effect on the net streamwise sediment flux. We note that the decrease in the relative wave contribution of the period-averaged sediment flux with increasing current strength was also reported for bed-load transport (Dohmen-Janssen et al., 2002).

3.4.2. Phase Variations in Near-Bed SSC

The net sediment entrainment rate indicates how the volume- or depth-averaged SSC changes in time. However, the local balance between diffusive, settling, and turbulent sediment fluxes governs the local SSC. Like bed shear stress and sediment entrainment, sediment concentrations near the bed significantly vary throughout the wave cycle. The phase evolution of the SSC within the water column is explained by examining the sediment fluxes governing $\langle\tilde{C}\rangle_p$. Planform and phase averaging the suspended sediment transport equation (equation (3)), and simplifying by recognizing $\tilde{C}' = \widetilde{u_i}' = 0$, and C_w, C_c, $u_{i,w}$, $u_{i,w}$, and w_s are independent of planform averaging, gives

$$\frac{\partial\langle\tilde{C}\rangle_p}{\partial t} = K\frac{\partial^2\langle\tilde{C}\rangle_p}{\partial z^2} + \frac{\partial}{\partial z}\left[w_s\langle\tilde{C}\rangle_p\right] - \frac{\partial}{\partial z}\left[\left\langle\widetilde{w'c'}\right\rangle_p\right] \tag{29}$$

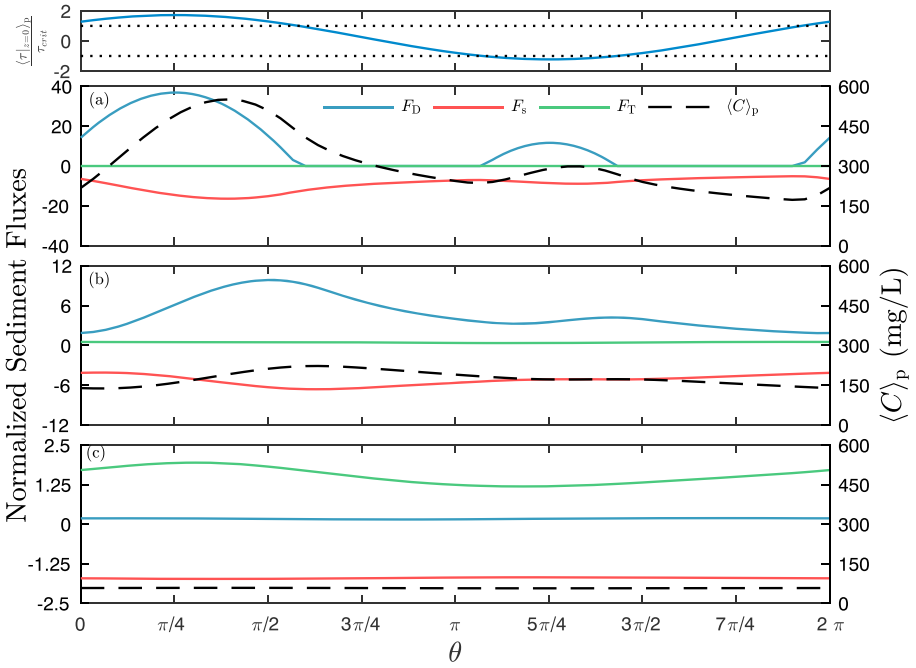

Figure 10. Phase evolution of the planform- and phased-averaged sediment concentration $\langle C_w \rangle_p$ (dashed lines) and sediment budget terms at (a) the bed, (b) the top of the viscous sublayer ($z^+ = 5$ or $z \approx 1\Delta$), and (c) the top of the buffer layer ($z^+ = 30$ or $z \approx 6\Delta$) for run 500WC. For reference, an insert of the bed shear stress is also included, where the dashed horizontal lines indicate $\pm\tau_{crit}$.

$$= -\frac{\partial F_D}{\partial z} - \frac{\partial F_s}{\partial z} - \frac{\partial F_T}{\partial z}, \tag{30}$$

where $F_T = (\widetilde{w'c'})_c + (\widetilde{w'c'})_w$, $F_s = -w_s(C_c + C_w)$, and $F_D = -K(\partial_z C_c + \partial_z C_w)$ are the total (combined current and wave components) turbulent, settling, and diffusive sediment fluxes, respectively. After noting that $\langle \tilde{C} \rangle_p = C_c + \langle C_w \rangle_p$, $\widetilde{w'c'} = (\widetilde{w'c'})_c + (\widetilde{w'c'})_w$, $\partial_t \langle \tilde{C} \rangle_p = \partial_t \langle \tilde{C}_w \rangle_p$, and canceling current terms, equation (29) becomes the governing equation for $\langle C_w \rangle_p$, viz.

$$\frac{\partial \langle C_w \rangle_p}{\partial t} = K \frac{\partial^2}{\partial z^2} \left[\langle C_w \rangle_p \right] + \frac{\partial}{\partial z} \left[w_s \langle C_w \rangle_p \right] - \frac{\partial}{\partial z} \left[\left\langle \left(\widetilde{w'c'} \right)_w \right\rangle_p \right]. \tag{31}$$

Despite this simplification, we examine the total fluxes in equation (29) to illustrate the net effect of diffusion, settling, and turbulence on SSC.

The phase evolution of the sediment fluxes and $\langle \tilde{C} \rangle_p$ are plotted at (a) the bed, (b) the top of the viscous sublayer ($z^+ = 5$ or $z \approx 1\Delta$ for run 500WC), and (c) the top of the buffer layer ($z^+ = 30$ or $z \approx 6\Delta$ for run 500WC) in Figure 10 for run 500WC. Trends are similar for runs 200WC and 350WC. We note that at the bed $F_D = \langle \tilde{E} \rangle_p$ and $F_s = \langle \tilde{D} \rangle_p$.

Early in the wave cycle, sediment entraining into the water column (Figure 10a) is vertically transported through the wave boundary layer by the diffusive flux. The pulse of eroded sediment takes a time of roughly $\Delta^2/(2K) = 1/\omega$ (since $K = \nu$) to be transported from the bed to $z = \Delta$ (Figure 10b). While $\langle \tilde{E} \rangle_p > 0$, SSC generally increases over the first Stokes layer thickness.

By $\theta \approx 3\pi/8$, the sediment depositional flux is larger than the erosional flux, and SSC at the bed decreases (Figure 10a). Sediment erosion is eliminated by $\theta \approx \pi/2$, and SSC at the bed exponentially decays. However, higher in the water column SSC continues to increase as the eroded pulse of sediment propagates upward. In addition to being vertically transported, both diffusion and turbulent mixing cause the sediment pulse to vertically spread as the wave cycle progresses. The spreading is evident by the broader SSC peak and magnitude reduction in F_D at the top of the viscous sublayer (Figure 10b). The vertical turbulent sediment flux quickly increases with height within the buffer layer. At $z^+ = 13$ ($z \approx 3\Delta$, not shown), the turbulent and diffusive fluxes are roughly equal in magnitude, and by the top of the buffer layer turbulent transport dominates

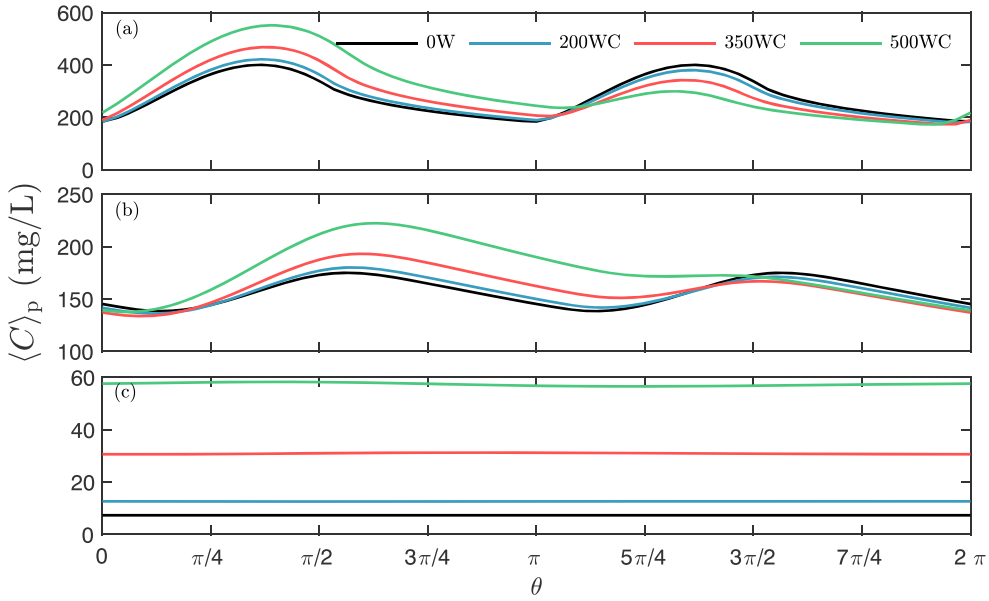

Figure 11. Phase evolution of the planform- and phased-averaged sediment concentration $\langle C_w \rangle_p$ at (a) the bed, (b) $z \approx 1\Delta$, and (c) $z \approx 6\Delta$ for runs 0W, 200WC, 350WC, and 500WC. The heights corresponding to each panel are identical to those in Figure 10.

the diffusive flux and is nearly balanced by the depositional flux (Figure 10c). Waves do not cause significant phase variations in the SSC at the top of the buffer layer.

The phase evolution of the sediment fluxes are similar during the adverse pressure gradient with three exceptions. (1) Because erosion decreases during the adverse pressure gradient, sediment fluxes (Figure 10) and concentrations are generally lower. (2) The duration in which the bed shear stress exceeds the critical shear stress also reduces, leading to less overall sediment suspension. (3) Finally, changes in the timing at which the bed shear stress exceeds and subsequently drops below the critical shear stress also slightly affects the phasing of the sediment budget.

Asymmetries in the sediment fluxes counterintuitively lead to larger sediment concentrations near the bed for weaker currents during the second half of the wave cycle. The phase evolution of the planform- and phased-averaged SSC for all runs is shown in Figure 11 at the same heights as Figure 10. Generally speaking, the effects of mixing by currents is indicated by the increased SSC for stronger currents. The sediment concentration peak at the bed during the second half of the wave cycle for the wave-only run is 25% larger than the peak for the case with the strongest currents (run 500WC; Figure 11a). However, the differences in SSC are much smaller by just one Stokes layer thickness from the bed. By $z = 6\Delta$, suspended sediment concentrations show no wave effects. Despite the strong effects on the SSC magnitude, phase variations in SSC are minimal for all runs.

4. Summary and Conclusions

We simulated shallow-water sediment dynamics in wave-dominated wave- and current-driven flows using DNS for conditions common in estuaries. The interaction between waves and currents and the resulting sediment transport mechanisms were investigated. Currents accelerated in the presence of laminar waves, a manifestation of reduced vertical turbulent momentum fluxes. For the simulated conditions, waves effectively reduced the bottom roughness and drag felt on the flow by the bed. These results suggest that the well-known enhanced roughness on the current boundary layer due to the presence of a turbulent wave boundary layer is not always applicable in fine sediment estuarine environments in which the wave boundary layer can be laminar.

Although waves modified currents, currents had little effect on the wave velocity field. Wave velocity profiles closely resemble Stokes solution for all runs. Similar behavior was observed for pulsating flow in channels (Scotti & Piomelli, 2001; Tardu & Binder, 1993) and pipes (Hwang & Brereton, 1991; Manna et al., 2012, 2015;

Ramaprian & Tu, 1983) when the wave boundary layer is smaller than the viscous sublayer associated with the mean flow.

Although the oscillatory nature of the waves led to a large bed shear stress that exceeded the critical shear stress of the sediment bed during portions of the wave cycle, the simulated wave boundary layer was laminar. Because currents did not significantly affect the wave field, the oscillating bed shear stress was in phase with the Stokes solution. Although currents do not affect phasing of the bed shear stress, they increase the magnitude by $\rho_0 u_*^2$. This increase modified the timing and duration in which the critical shear stress of the sediment bed was exceeded. Stronger currents increase the sediment entrainment when the wave pressure gradient drives flow in the direction of the currents. The opposite is true when the wave pressure gradient is adverse to the currents, leading to phase asymmetries in SSC profiles. Near-bed sediment concentrations are higher for weaker currents when the wave pressure gradient is adverse. This behavior may be an important consideration in benthic health models for species that are susceptible to SSC changes.

The waves controlled the phase evolution of near-bed SSC profiles. However, above $z = 5\Delta$, planform- and phased-averaged SSC for all conditions tested was within 2% of the period-averaged SSC throughout the wave cycle. Near $z^+ = 13$, vertical turbulent sediment fluxes became important. Throughout much of the water column, upward turbulent fluxes were balanced by downward settling fluxes. This balance is analogous to what occurs for sediment transport in pure currents (i.e., no waves). Simulated planform- and time-averaged SSC profiles closely resembled the equivalent Rouse profiles, wherein sediment was transported higher into the water column by stronger vertical turbulent mixing due to stronger currents.

Our results support the conceptual model that wind waves propagating into shallow waters with hydraulically smooth beds are responsible for mobilizing sediment, but in the absence of currents, vertical transport is weak and sediment remains in or near the wave boundary layer. However, the addition of even weak currents generates turbulence that transports sediment out of the wave boundary layer into the overlying water column. Field observations of sediment fluxes in South San Francisco Bay support this conclusion (Brand et al., 2010). For the conditions simulated, currents alone were not capable of suspending sediment, although SSC increased with stronger currents due to the associated increase in vertical turbulent mixing.

Acknowledgments
K. S. N. gratefully acknowledges the Charles H. Leavell Graduate Student Fellowship. K. S. N. and O. B. F. acknowledge the Stanford Woods Institute for the Environment and Office of Naval Research (ONR) grant N00014-15-1-2287. Presented data can be found at osf.io/j7puc.

References

Balachandar, S., & Eaton, J. K. (2010). Turbulent dispersed multiphase flow. *Annual Review of Fluid Mechanics*, *42*, 111–133.
Birman, V. K., Martin, J. E., & Meiburg, E. (2005). The non-Boussinesq lock-exchange problem. Part 2. High-resolution simulations. *Journal of Fluid Mechanics*, *537*, 125–144.
Bonometti, T., & Balachandar, S. (2008). Effect of Schmidt number on the structure and propagation of density currents. *Theoretical and Computational Fluid Dynamics*, *22*(5), 341–361.
Brand, A., Lacy, J. R., Gladding, S., Holleman, R., & Stacey, M. (2015). Model-based interpretation of sediment concentration and vertical flux measurements in a shallow estuarine environment. *Limnology and Oceanography*, *60*(2), 463–481. https://doi.org/10.1002/lno.10047
Brand, A., Lacy, J. R., Hsu, K., Hoover, D., Gladding, S., & Stacey, M. T. (2010). Wind-enhanced resuspension in the shallow waters of South San Francisco Bay: Mechanisms and potential implications for cohesive sediment transport. *Journal of Geophysical Research*, *115*, C11024. https://doi.org/10.1029/2010JC006172
Cantero, M. I., Balachandar, S., Cantelli, A., Pirmez, C., & Parker, G. (2009). Turbidity current with a roof: Direct numerical simulation of self-stratified turbulent channel flow driven by suspended sediment. *Journal of Geophysical Research*, *114*, 1–20. https://doi.org/10.1029/2008JC004978
Cantero, M. I., Balachandar, S., & Parker, G. (2009). Direct numerical simulation of stratification effects in a sediment-laden turbulent channel flow. *Journal of Turbulence*, *10*, N27.
Chen, S.-N., Sanford, L. P., & Ralston, D. K. (2009). Lateral circulation and sediment transport driven by axial winds in an idealized, partially mixed estuary. *Journal of Geophysical Research*, *114*, 1–18. https://doi.org/10.1029/2008JC00501
Cheng, Z., Yu, X., Hsu, T.-J., Ozdemir, C. E., & Balachandar, S. (2015). On the transport modes of fine sediment in the wave boundary layer due to resuspension/deposition: A turbulence-resolving numerical investigation. *Journal of Geophysical Research: Oceans*, *120*, 1918–1936. https://doi.org/10.1002/2014JC010623
Chou, Y.-J., & Fringer, O. B. (2010). A model for the simulation of coupled flow-bed form evolution in turbulent flows. *Journal of Geophysical Research*, *115*, 1–20. https://doi.org/10.1029/2010JC006103
Chou, Y.-J., Wu, F.-C., & Shih, W.-R. (2014). Toward numerical modeling of fine particle suspension using a two-way coupled Euler-Euler model. Part 1: Theoretical formulation and implications. *International Journal of Multiphase Flow*, *64*, 35–43.
Christie, M. C., Dyer, K. R., & Turner, P. (1999). Sediment flux and bed level measurements from a macro tidal mudflat. *Estuarine, Coastal and Shelf Science*, *49*(5), 667–688.
Christoffersen, J. B., & Jonsson, I. G. (1985). Bed friction and dissipation in a combined current and wave motion. *Ocean Engineering*, *12*(5), 387–423.
Cloern, J. E. (1987). Turbidity as a control on phytoplankton biomass and productivity in estuaries. *Continental Shelf Research*, *7*(11-12), 1367–1381.
Colijn, F. (1982). Light absorption in the waters of the Ems-Dollard estuary and its consequences for the growth of phytoplankton and microphytobenthos. *Netherlands Journal of Sea Research*, *15*(2), 196–216. https://doi.org/10.1016/0077-7579(82)90004-7
Cui, A. (1999). On the parallel computation of turbulent rotating stratified flows (PhD Thesis), Stanford University, Stanford, CA, USA.
Davis, R. H. (1996). Hydrodynamic diffusion of suspended particles: A symposium. *Journal of Fluid Mechanics*, *310*, 325–335.

del Alamo, J. C., Jiménez, J., Zandonade, P., & Moser, R. D. (2004). Scaling of the energy spectra of turbulent channels. *Journal of Fluid Mechanics*, *500*, 135–144.
Dohmen-Janssen, C. M., Kroekenstoel, D. F., Hassan, W. N., & Ribberink, J. S. (2002). Phase lags in oscillatory sheet flow: Experiments and bed load modelling. *Coastal Engineering*, *46*(1), 61–87.
Dyer, K. R., Christie, M. C., Feates, N, Fennessy, M. J., Pejrup, M., & Van der Lee, W. (2000). An investigation into processes influencing the morphodynamics of an intertidal mudflat, the Dollard Estuary, the Netherlands: I. Hydrodynamics and suspended sediment. *Estuarine, Coastal and Shelf Science*, *50*(5), 607–625.
Friedrichs, C. T. (2011). Tidal flat morphodynamics: A synthesis. In D. S. McLusky & E. Wolanski (Eds.), *Treatise on Estuarine and Coastal Science* (Chap. 3, pp. 137–170). Cambridge: Academic Press.
Glenn, S. M., & Grant, W. D. (1987). A suspended sediment stratification correction for combined wave and current flows. *Journal of Geophysical Research*, *84*(C8), 8244–8264.
Grant, W. D., & Madsen, O. S. (1979). Combined wave and current interaction with a rough bottom. *Journal of Geophysical Research*, *84*(C4), 1797–1808.
Green, M. O., & Coco, G. (2014). Review of wave-driven sediment resuspension and transport in estuaries. *Reviews of Geophysics*, *52*(1), 77–117.
Gundogdu, M. Y., & Carpinlioglu, M. O. (1999a). Present state of art on pulsatile flow theory: Part 1: Laminar and transitional flow regimes. *JSME International Journal Series B*, *42*(3), 384–397.
Gundogdu, M. Y., & Carpinlioglu, M. O. (1999b). Present state of art on pulsatile flow theory: Part 2: Turbulent flow regime. *JSME International Journal Series B*, *42*(3), 398–410.
Hill, P. S., Voulgaris, G., & Trowbridge, J. H. (2001). Controls on floc size in a continental shelf bottom boundary layer. *Journal of Geophysical Research*, *106*(C5), 9543.
Hino, M., Sawamoto, M., & Takasu, S. (1976). Experiments on transition to turbulence in an oscillatory pipe flow. *Journal of Fluid Mechanics*, *75*(2), 193–207.
Hwang, J.-L., & Brereton, G. (1991). Turbulence in high-frequency periodic fully-developed pipe flow. In *8th Symposium on Turbulent Shear Flows* (Vol. *1*, pp. 11–3). Munich, Germany.
Jones, C. A., & Jaffe, B. E. (2013). Influence of history and environment on the sediment dynamics of intertidal flats. *Marine Geology*, *345*, 294–303.
Kim, J., & Moin, P. (1985). Application of a fractional-step method to incompressible Navier-Stokes equations. *Journal of Computational Physics*, *59*(2), 308–323.
Kirk, J. (1985). Effects of suspensoids (turbidity) on penetration of solar radiation in aquatic ecosystems. *Hydrobiologia*, *125*(1), 195–208. https://doi.org/10.1007/BF00045935
Lacy, J. R., Gladding, S., Brand, A., Collignon, A., & Stacey, M. (2014). Lateral baroclinic forcing enhances sediment transport from shallows to channel in an estuary. *Estuaries Coasts*, *37*(5), 1058–1077.
Lee, M., & Moser, R. D. (2015). Direct numerical simulation of turbulent channel flow up to $Re_\tau = 5200$. *Journal of Fluid Mechanics*, *774*, 395–415.
Leonard, B. P. (1979). A stable and accurate convective modelling procedure based on quadratic upstream interpolation. *Computer Methods in Applied Mechanics*, *19*(1), 59–98.
Leonard, B. (1988). Simple high-accuracy resolution program for convective modelling of discontinuities. *International Journal for Numerical Methods in Fluids*, *8*(10), 1291–1318.
Lick, W. (2008). *Sediment and Contaminant Transport in Surface Waters*. Boca Raton, FL: CRC Press.
Lodahl, C., Sumer, B. M., & Fredsøe, J. (1998). Turbulent combined oscillatory flow and current in a pipe. *Journal of Fluid Mechanics*, *373*, 313–348.
MacVean, L. J., & Lacy, J. R. (2014). Interactions between waves, sediment, and turbulence on a shallow estuarine mudflat. *Journal of Geophysical Research: Oceans*, *119*, 1534–1553. https://doi.org/10.1002/2013JC009477
Manna, M., Vacca, A., & Verzicco, R. (2012). Pulsating pipe flow with large-amplitude oscillations in the very high frequency regime. Part 1. Time-averaged analysis. *Journal of Fluid Mechanics*, *700*, 246–282.
Manna, M., Vacca, A., & Verzicco, R. (2015). Pulsating pipe flow with large-amplitude oscillations in the very high frequency regime. Part 2. Phase-averaged analysis. *Journal of Fluid Mechanics*, *766*, 272–296.
Manning, A., & Schoellhamer, D. (2013). Factors controlling floc settling velocity along a longitudinal estuarine transect. *Marine Geology*, *345*, 266–280.
Moin, P., & Kim, J. (1982). Numerical investigation of turbulent channel flow. *Journal of Fluid Mechanics*, *118*, 341–377.
Necker, F., Härtel, C., Kleiser, L., & Meiburg, E. (2005). Mixing and dissipation in particle-driven gravity currents. *Journal of Fluid Mechanics*, *545*, 339–372.
Nelson, K. S., & Fringer, O. B. (2017). Reducing spin-up time for simulations of turbulent channel flow. *Physics of Fluids*, *29*(10), 105101.
Nielsen, P. (1992). *Coastal Bottom Boundary Layers and Sediment Transport*, (Vol. 4). Singapore: World scientific.
Ozdemir, C. E., Hsu, T.-J., & Balachandar, S. (2010a). A numerical investigation of fine particle laden flow in an oscillatory channel: The role of particle-induced density stratification. *Journal of Fluid Mechanics*, *665*, 1–45.
Ozdemir, C. E., Hsu, T.-J., & Balachandar, S. (2010b). Simulation of fine sediment transport in oscillatory boundary layer. *Journal of Hydro-environment Research*, *3*(4), 247–259.
Parchure, T. M., & Mehta, A. J. (1985). Erosion of soft cohesive sediment deposits. *Journal of Hydraulic Engineering*, *111*(10), 1308–1326.
Pope, S. B. (2000). *Turbulent Flows*. Cambridge, United Kingdom: Cambridge University Press.
Pritchard, D., & Hogg, A. J. (2003). Cross-shore sediment transport and the equilibrium morphology of mudflats under tidal currents. *Journal of Geophysical Research*, *108*(C10), 1–15. https://doi.org/10.1029/2002JC001570
Ramaprian, B., & Tu, S.-W. (1980). An experimental study of oscillatory pipe flow at transitional Reynolds numbers. *Journal of Fluid Mechanics*, *100*(3), 513–544.
Ramaprian, B., & Tu, S. (1983). Fully developed periodic turbulent pipe flow. Part 2. The detailed structure of the flow. *Journal of Fluid Mechanics*, *137*, 59–81.
Sanford, L. P. (1994). Wave-forced resuspension of upper Chesapeake Bay muds. *Estuaries*, *17*(1), 148–165.
Sanford, L. P. (2008). Modeling a dynamically varying mixed sediment bed with erosion, deposition, bioturbation, consolidation, and armoring. *Computers & Geosciences*, *34*(10), 1263–1283.
Sanford, L. P., & Maa, J. P.-Y. (2001). A unified erosion formulation for fine sediments. *Marine Geology*, *179*(1), 9–23.
Sarpkaya, T. (1966). Experimental determination of the critical Reynolds number for pulsating Poiseuille flow. *Journal of Basic Engineering*, *88*(3), 589–598.

Schultz, M. P., & Flack, K. A. (2013). Reynolds-number scaling of turbulent channel flow. *Physics of Fluids*, *25*(2), 025104.
Scotti, A., & Piomelli, U. (2001). Numerical simulation of pulsating turbulent channel flow. *Physics of Fluids*, *13*(5), 1367–1384.
Segre, P. N., Liu, F., Umbanhowar, P., & Weitz, D. A. (2001). An effective gravitational temperature for sedimentation. *Nature*, *409*(6820), 594.
Singer, B. A., Ferziger, J. H., & Reed, H. L. (1989). Numerical simulations of transition in oscillatory plane channel flow. *Journal of Fluid Mechanics*, *208*, 45–66.
Styles, R., & Glenn, S. M. (2000). Modeling stratified wave and current bottom boundary layers on the continental shelf. *Journal of Geophysical Research*, *105*(C10), 24,119–24,139.
Styles, R., Glenn, S. M., & Brown, M. E. (2017). An optimized combined wave and current bottom boundary layer model for arbitrary bed roughness (Tech. Rep.) Vicksburg, United States: ERDC-CHL.
Tardu, F. S., & Binder, G. (1993). Wall shear stress modulation in unsteady turbulent channel flow with high imposed frequencies. *Physics of Fluids A: Fluid*, *5*(8), 2028–2037.
Warner, J. C., Sherwood, C. R., Signell, R. P., Harris, C. K., & Arango, H. G. (2008). Development of a three-dimensional, regional, coupled wave, current, and sediment-transport model. *Computers & Geosciences*, *34*(10), 1284–1306.
Yeh, T.-h., Cantero, M., Cantelli, A., Pirmez, C., & Parker, G. (2013). Turbidity current with a roof: Success and failure of RANS modeling for turbidity currents under strongly stratified conditions. *Journal of Geophysical Research: Earth Surface*, *118*, 1975–1998. https://doi.org/10.1002/jgrf.20126
Yu, X., Ozdemir, C., Hsu, T.-J., & Balachandar, S. (2013). Numerical investigation of turbulence modulation by sediment-induced stratification and enhanced viscosity in oscillatory flows. *Journal of Waterway, Port, Coastal, and Ocean ASCE*, *140*(2), 160–172.
Zang, Y., Street, R. L., & Koseff, J. R. (1994). A non-staggered grid, fractional step method for time-dependent incompressible Navier-Stokes equations in curvilinear coordinates. *Journal of Computational Physics*, *114*(1), 18–33.
Zedler, E. A., & Street, R. L. (2001). Large-eddy simulation of sediment transport: Currents over ripples. *Journal of Hydraulic Engineering*, *127*, 444–452.
Zedler, E. A., & Street, R. L. (2006). Sediment transport over ripples in oscillatory flow. *Journal of Hydraulic Engineering*, *132*(2), 180–193.